Siyuan Zhang[a], Hamidreza Hajiyani[a], Alexander G. Hufnagel[a,b], Jonathan Kampmann, Benjamin Breitbach, Thomas Bein, Dina Fattakhova-Rohlfing, Rossitza Pentcheva and Christina Scheu*

Sn-Doped Hematite for Photoelectrochemical Water Splitting: The Effect of Sn Concentration

https://doi.org/10.1515/zpch-2019-1482
Received May 15, 2019; accepted October 11, 2019

Abstract: Hematite-based photoanodes have been intensively studied for photoelectrochemical water oxidation. The *n*-type dopant Sn has been shown to benefit the activity of hematite anodes. We demonstrate in this study that Sn-doped hematite thin films grown by atomic layer deposition can achieve uniform doping across the film thickness up to at least 32 mol%, far exceeding the equilibrium solubility limit of less than 1 mol%. On the other hand, with the introduction of Sn doping, the hematite crystallite size decreases and many twin boundaries form in the film, which may contribute to the low photocurrent observed in these films. Density functional theory calculations with a Hubbard *U* term show that Sn doping has multiple effects on the hematite properties. With increasing Sn^{4+}

[a] **Siyuan Zhang, Hamidreza Hajiyani and Alexander G. Hufnagel:** These authors contributed equally to this work.
[b] Current Address: BASF SE, Carl-Bosch-Straße 38, 67056 Ludwigshafen, Germany
***Corresponding author: Christina Scheu,** Max-Planck-Institut für Eisenforschung GmbH, Max-Planck-Straße 1, 40237 Düsseldorf, Germany, e-mail: c.scheu@mpie.de
Siyuan Zhang and Benjamin Breitbach: Max-Planck-Institut für Eisenforschung GmbH, Max-Planck-Straße 1, 40237 Düsseldorf, Germany
Hamidreza Hajiyani and Rossitza Pentcheva: Department of Physics and Center for Nanointegration Duisburg-Essen (CENIDE), Universität Duisburg-Essen, Lotharstraße 1, 47057 Duisburg, Germany
Alexander G. Hufnagel, Jonathan Kampmann and Thomas Bein: Department of Chemistry and Center for NanoScience (CeNS), University of Munich (LMU), Butenandtstraße 5-13 (E), 81377 Munich, Germany
Dina Fattakhova-Rohlfing: Institute of Energy and Climate Research (IEK-1), Forschungszentrum Jülich GmbH, Wilhelm-Johnen-Straße, 52425 Jülich, Germany; and Faculty of Engineering and Center for Nanointegration Duisburg-Essen (CENIDE), Universität Duisburg-Essen, Lotharstraße 1, 47057 Duisburg, Germany

content, the Fe^{2+} concentration increases, leading to a reduction of the band gap and finally to a metallic state. This goes hand in hand with an increase of the lattice constant.

Keywords: atomic layer deposition; density functional theory calculation; hematite thin film electrode; photoelectrochemical water splitting; twin boundary.

1 Introduction

Hematite (α-Fe_2O_3) has long been studied for photoelectrochemical (PEC) water oxidation [1–16]. It has a suitable band gap of ~2.1 eV for solar light absorption, a high absorption coefficient and an adequate band alignment to drive the demanding water oxidation reaction [2]. The fundamental limit of hematite, like many other transition metal oxides, is its poor conductivity. Both types of charge carriers, electrons and holes, are highly localized in space, and transport occurs by a phonon-assisted polaron mechanism. For *n*-type hematite photoanodes, the minority carrier hole has a diffusion length of only 2–4 nm [3] and is hence very prone to recombination. Therefore, only the photogenerated holes originating in the top few nanometers of a hematite layer can reach the interface for the water oxidation reaction.

Nanostructuring hematite photoanodes [2, 4–7] is a common strategy to remedy the limited hole diffusion length by providing a shorter transport path for the photogenerated holes to reach the interface. Nevertheless, it is difficult to design nanostructures with a critical dimension matching the hole diffusion length. In addition, the conductivity may be further compromised by the surface and by crystallographic defects in the bulk [6], and quantum confinement may alter the band structure and alignment [7].

Another possibility is to improve the transport properties of hematite by substituting other elements [8], such as Al, Si, Ti, Cr, Ni, Cu, Zn, Zr, Nb, Mo, Sn, Pt, as has been summarized in a previous report [9]. In a recent study, Sn doping was demonstrated to have the highest photocurrent and the lowest photovoltage onset among other commonly studied *n*-type dopants [10]. Improving the *n*-type conductivity in a photoanode not only improves the current collection through the substrate, but also reduces the probability of recombination with holes. It is noteworthy that Sn has either been doped into hematite by the addition of a chemical precursor [9–12], or through diffusion from the fluorine doped tin oxide (FTO) substrate via annealing at high temperatures [13–15]. In our recent study [16], we have identified two beneficial effects of Sn in the hematite lattice. Sn-doped

hematite with <20 nm thickness has been fabricated by atomic layer deposition (ALD), which is ultrathin and yet capable of absorbing 44% of the incident solar photons with an energy above the band gap. By introducing Sn doping at different locations of the films, it has been established that Sn doping on the surface and in the ~5 nm subsurface volume has a beneficial effect on the transport properties. In combination with first principles electronic structure calculations, Sn doping on the surface was shown to improve the interface activity by passivating surface trap states, while the subsurface doping was responsible for an improved charge separation by inducing a band edge gradient. In contrast, doping Sn throughout the thickness of the film does not translate to improved efficiency.

For screening the effect of doping elements, the doping concentration rarely exceeds 1–5 mol%. One practical constraint is the solubility of foreign atoms in the hematite structure [8]. For example, SnO_2 has a very limited solubility in hematite, less than 1 mol% below 800 °C [17]. A higher solubility of 6 mol% [18] and 20 mol% [17] of SnO_2 has been demonstrated in hematite nanoparticles, which found applications in the gas sensor industry [17]. ALD is a powerful technique to deposit films that are far from their thermal equilibrium. In this study, we demonstrate that Sn can be incorporated into the hematite crystal structure at a concentration as high as 32 mol%. Hematite thin films with 6, 14, and 32 mol% Sn concentrations were studied by X-ray diffraction (XRD), scanning transmission electron microscopy (STEM) and spectroscopy, and their structural and electronic characteristics were correlated to density functional theory (DFT) calculations. The photocurrents derived from hematite photoanodes peak at low Sn concentration, and vanish as the Sn concentration exceeds 32 mol%.

2 Experimental

2.1 Preparation of photoanodes

The oxide films were deposited on FTO-coated glass substrates (Pilkington, 7 Ω per square), prepared by successive sonication in Extran (Merck) solution, ultrapure water (MilliQ, 18.2 MΩ cm), and 2-propanol for 15 min and drying in a stream of nitrogen. Single side polished Si (100) wafers (Siltronic AG) were used as substrates for microstructural characterization (Section 2.2). Ferrocene (Aldrich, 98%) was purified by sublimation prior to use.

A Picosun R-200 Advanced ALD system was used for all depositions. The chamber temperature was 250 °C at a pressure of approximately 10 hPa. Nitrogen

(Air Liquide, 99.999%) was used at a constant flow rate of 100 sccm per precursor feed line and 150 sccm for the reactor chamber as a carrier and purge gas. Hematite was deposited by alternating between exposures to ferrocene, kept in a stainless steel cylinder at 90 °C, and ozone, produced by an INUSA AC2025 ozone generator fed with 1 vol% N_2 in O_2 (Air Liquide, 99.9995%). One full cycle consisted of a 1 s ferrocene pulse, 6 s purge, 6 s ozone pulse and a final 8 s purge. Tin oxide was deposited from $SnCl_4$ (SAFC electronic grade) and MilliQ water, both kept in stainless steel cylinders at 18 °C. One deposition cycle consisted of a 0.1 s $SnCl_4$ pulse, 6 s purge, 15 s water pulse and final 8 s purge. Mixed oxide films were prepared interspersing one cycle of tin oxide after every *N* cycles of hematite, resulting in films with an ALD cycle ratio of the two oxides of 1:*N*, which is used to identify samples throughout this study. This was done by alternating between *N* hematite deposition cycles and one tin oxide cycle until 1000 hematite cycles were reached, then capping with another *N* hematite cycles. A thicker pure hematite film was grown for structural characterization using 1600 cycles, consisting of a 1.5 s ferrocene pulse, 7 s static exposure and 8 s purge, followed by a 6 s ozone pulse, 7 s static exposure and 8 s purge. After deposition, the films were annealed in air at 600 °C for 30 min with a heating rate of 3.2 °C/min, and then cooled naturally to room temperature.

Higher Sn concentration is achieved by higher ALD cycle ratios 1:*N*, i.e. lower number of hematite cycles, *N*, in between the tin oxide cycles. The ALD growth rate of hematite using the chemistry above are approximately 0.025 nm/cycle. However, the growth rate of doped films can deviate significantly, as hematite and tin oxide undergo heterogeneous nucleation on each other, which may be subject to delaying or promoting effects of the substrate.

2.2 Microstructural characterization

XRD was performed using a Rigaku SmartLab 9 kW X-ray diffractometer with a Cu–Kα (1.54056 Å) radiation source produced at 45 kV and 200 mA, a parallel beam optic and an energy-dispersive line detector. The in-plane 2θ scan was configured using the 5-circle goniometer with a scan speed of 2°/min and 0.12° per 2θ step. For the in-plane diffraction, both the incident and diffracted beams are nearly parallel to the sample surface, so that the penetration depth of the beam is within 100 nm of the surface. The technique measures lattice planes that are nearly perpendicular to the sample surface. Simulation of the X-ray pattern was performed using the Bruker TOPAS software for the fundamental parameter fit (Pawley method). Pole figures of hematite thin films were recorded on a Seifert Theta/Theta diffractometer with a Co–Kα (1.78897 Å) radiation source

produced at 40 kV and 30 mA, a parallel beam optic and an energy-dispersive point detector.

Further microstructure characterization was conducted in a Titan Themis microscope operated at 300 kV. Aberration correction of the probe-forming lenses enables a probe size of <1 Å and a convergence semi-angle of 23.8 mrad. High angle annular dark field (HAADF) and annular bright field (ABF) micrographs were collected using annular detectors with collection semi-angles in the range of 73–200 mrad and 8–16 mrad, respectively. Energy dispersive spectroscopy (EDS) was done using a SuperX Si drift detector. Elemental quantification was performed using the Bruker Espirit software by the standardless Cliff-Lorimer method. Electron energy loss spectroscopy (EELS) was conducted using a Gatan Quantum ERS spectrometer operated in the image-coupled mode with a collection semi-angle up to 35 mrad.

2.3 Optical characterization

UV-Vis absorption data of hematite film electrodes were obtained on a Perkin Elmer Lambda 1050 UV/Visible/NIR spectrophotometer combined with an integrating sphere. The intrinsic absorbance of the films was calculated by applying an expression derived by Klahr et al. [19], which corrects for substrate absorption as well as substrate and film reflectance.

2.4 Photoelectrochemistry

PEC measurements were performed in a 20 cm^3 optical glass three-electrode cell with 0.1 M NaOH as the electrolyte. The oxide film was masked with polytetrafluoroethene adhesive tape to limit the exposed area to 0.159 cm^2, contacted with silver paste and used as the working electrode. For cyclovoltammetry (CV) measurements, the film was connected as working electrode to a Metrohm PGStat302N potentiostat. Additionally, a Pt wire counter electrode and a saturated Ag/AgCl reference electrode (Sigma Aldrich, 0.197 V vs. standard hydrogen electrode) were used to apply defined potential sweeps and to record the resulting current in a three electrode setup. CV measurements were performed at a scan rate of 20 mV s^{-1}. The potential vs. reversible hydrogen electrode (RHE) in V was calculated from the measured potential vs. Ag/AgCl at pH = 13 according to the equation: $V_{RHE} = 0.197 + 0.059\ pH$.

The film was illuminated from the front side by a blue light emitting diode (Thorlabs, 455 nm). The flux incident on the electrode was set to be 10^{17} cm^{-2} s^{-1} at the sample position prior to each measurement using a certified Fraunhofer ISE silicon reference cell with a KG5 IR-cutoff filter.

2.5 Computational details

DFT calculations were carried out with the VASP code, which uses the projected augmented wave (PAW) method, and pseudopotentials [20–23]. We also adopted the generalized-gradient approximation (GGA-PBE96) [24] for the exchange correlation functional and an effective Hubbard value $U - J = 4.3$ eV to describe static electronic correlations of the *3d* states of Fe using Dudarev's approach [25]. For converged results, we used a plane-wave cut-off of 500 eV and a Monkhorst–Pack *k*-point mesh of $7 \times 7 \times 4$ [26]. A full relaxation of the unit cell and the ionic positions was performed until the residual forces were less than 0.01 eV $Å^{-1}$.

3 Results and discussion

3.1 Atomic layer deposition of Sn-doped hematite

3.1.1 Phase

Hematite has a trigonal structure (space group R-3c, number 167), an isostructure to corundum (α-Al_2O_3). The hexagonal unit cell is conventionally used, so are the hexagonal Miller-Bravais indices (*h*, *k*, *i*, *l*) to label the diffraction. We use the full 4 indices in this manuscript, whereas most studies omit the dummy index $i = -h - k$. Note however, the rhombohedral index also uses 3 indices, but they are defined using the rhombohedral unit cell. The conversion between the 2 systems of the low-index lattice planes is listed in Table 1.

XRD characterization was conducted on the ultrathin hematite films grown on flat Si (100) substrates. A fiber texture has been demonstrated for undoped hematite [16] with the plane normal of Fe_2O_3 (0,0,0,6) (*c*-plane) parallel to the growth direction. In order to maximize the signal from the ultrathin films, we applied the in-plane diffraction geometry with grazing incidence, while collecting diffractions only from planes 90° to the growth direction due to the fiber texture. As shown in Table 1 and Figure 1a, the peaks observed in this geometry are all in-plane reflections, including (1,1,−2,0), (3,0,−3,0), and (2,2,−4,0).

As the concentration of Sn increases, no new reflections have been identified. This may suggest the absence of crystalline phases other than hematite, but cannot exclude the formation of crystalline phases with a different texture and hence not contributing to in-plane diffraction. The (1,1,−2,0) reflection shifts monotonically to the left as the Sn concentration increases, indicating an expansion of the lattice parameter *a*, which is summarized in Table 2.

Tab. 1: Conversion between the hexagonal Miller-Bravais index and the rhombohedral index of the low-index hematite planes, and their inclination angles to the *c*-plane normal (growth direction of the fiber textured film).

2θ (°)	Plane spacing (Å)	Hexagonal index	Rhombohedral index	Inclination to the growth direction (°)
24.0	3.70	(0,1,−1,2)	(1,1,0)	58
33.0	2.71	(1,0,−1,4)	(2,1,1)	38
35.4	2.53	**(1,1,−2,0)**	**(1,0,−1)**	**90**
39.0	2.30	(0,0,0,6)	(2,2,2)	0
40.6	2.22	(1,1,−2,3)	(2,1,0)	61
43.3	2.09	(2,0,−2,2)	(2,0,0)	72
49.2	1.85	(0,2,−2,4)	(2,2,0)	58
53.7	1.70	(1,1,−2,6)	(3,2,1)	42
57.1	1.61	(1,2,−3,2)	(2,1,−1)	77
57.2	1.61	(0,1,−1,8)	(3,3,2)	22
62.1	1.49	(2,1,−3,4)	(3,1,0)	64
63.6	1.46	**(3,0,−3,0)**	**(2,−1, −1)**	**90**
69.1	1.36	(2,0,−2,8)	(4,2,2)	38
71.5	1.32	(1,0,−1,10)	(4,3,3)	18
71.8	1.31	(1,1,−2,9)	(4,3,2)	31
75.0	1.27	**(2,2,−4,0)**	**(2,0,−2)**	**90**

The in-plane reflections are highlighted in bold.

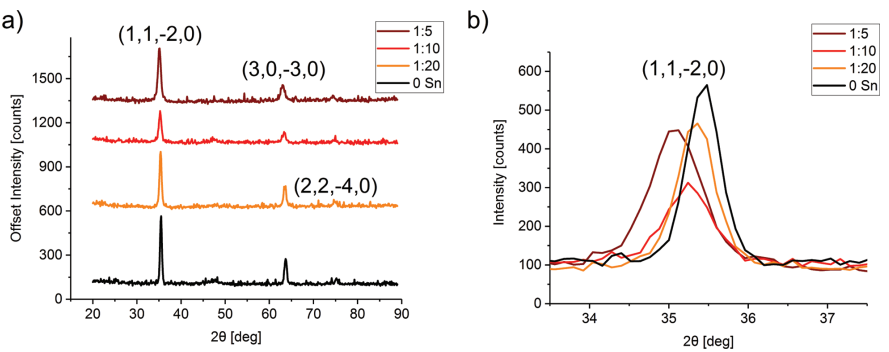

Fig. 1: (a) In-plane XRD of Sn-doped hematite with various ALD cycle ratios and (b) the enlarged view on the (1,1,−2,0) reflection.

3.1.2 Chemical composition

The chemical composition of the thin films and their homogeneity were studied by EDS and EELS in STEM. It has been noted in our earlier study [27] that due to the

Tab. 2: Summary of Sn-doped hematite thin films with various ALD cycle ratios: Chemical composition (EDS), lattice parameters (XRD), chemical shift of Fe-L_3 edge (EELS) and the deduced Fe^{2+} concentration.

ALD cycle ratio	Sn (mol%)[a]	*a* (Å)	Fe-L_3 edge (eV)[b]	Fe^{2+} (mol%)[a]
0	0	5.0629 ± 0.0006	710.22 ± 1.37	0
1:20	6	5.0766 ± 0.0007	710.12 ± 1.47	6
1:10	14	5.0893 ± 0.0013	710.08 ± 1.74	8
1:5	32	5.1129 ± 0.0010	710.02 ± 1.57	12

[a]A relative error of $\pm 5\%$ can be considered as a systematic error from Cliff-Lorimer quantification of Sn. An absolute error of ± 1 mol% can be taken for the quantification of Fe^{2+}, considering a pixel-precision, 0.05 eV, of the Fe-L_3 edge.
[b]The notation $\pm$ in this column does not refer to uncertainty, rather the width (1 standard deviation) of the peak from a Gaussian profile fitting.

fluorescence artefact of Sn from the FTO substrate, EDS is inappropriate to quantify small amounts of Sn in the hematite thin film. In this study, we quantify Sn in the hematite films grown on the Si (100) substrate so that the fluorescence artefact is no longer a concern. As shown in Table 2, the Sn concentration increases as the ALD cycle ratio of 1 cycle of SnO_2 per *N* cycles of Fe_2O_3 (abbreviated 1:*N*) increases, i.e. tin oxide layers are separated by fewer layers of iron oxide. A high Sn concentration of 32 mol% is reached at the ratio of 1:5, approximating to the chemical formula $SnFe_2O_x$. Even at this composition, a homogeneous distribution of Fe and Sn throughout the film thickness is evidenced in Figure 2b, and there is no indication of a second phase. Homogeneous doping of Sn is further evidenced by the monotonous expansion of the in-plane lattice parameter *a*. With the Sn concentrations evaluated by EDS, a linear expansion of *a* is evaluated as 0.03% per mol% of Sn. This is comparable to the evaluation from Sn-doped hematite nanoparticles [17] where both lattice parameters *a* and *c* expand by 0.02% per mol% of Sn.

The incorporation of Sn is further evidenced by the EELS Sn-$M_{4,5}$ edge (Figure 2c) and the effect of Sn on the oxidation state of Fe. As discussed in a previous work, a shift of the EELS Fe-L_3 edge (Figure 2d) towards lower energy loss corresponds to the reduction of Fe^{3+} [27]. Integrating the EELS spectra from within Sn-doped hematite, a monotonic shift of the Fe-L_3 position is observed towards lower energy loss. This is in agreement with theoretical studies [9, 16] that suggest that Fe atoms adjacent to substitutional Sn^{4+} atoms can be reduced to a Fe^{2+} state. In Sn-doped hematite, the Fe L_3 edge is a superposition of the Fe^{3+} and Fe^{2+} spectra. Hence, a shift of the peak centroid towards lower energy loss is expected together with a broadening of the profile, as shown in Figure 2c and Table 2. Fe^{3+} and Fe^{2+} minerals were characterized to have a 1.7 eV difference in the Fe-L_3

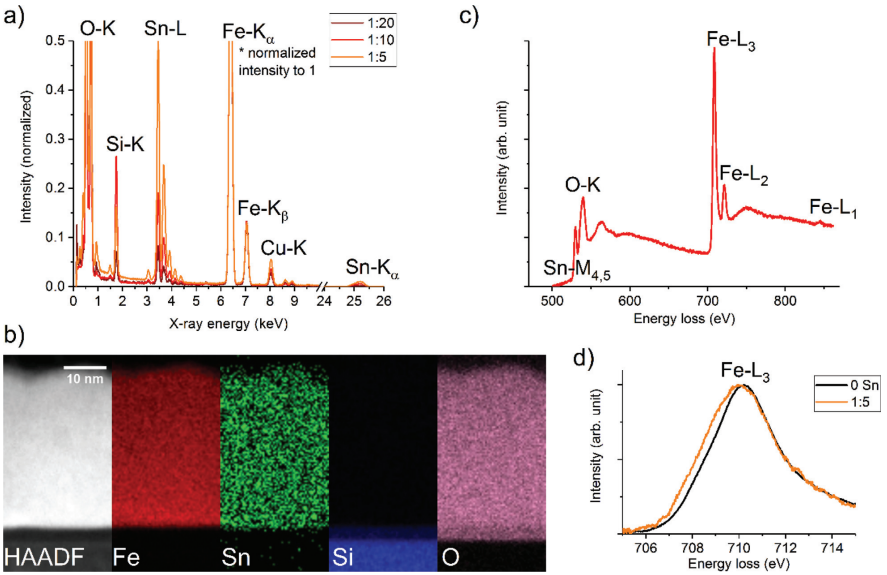

Fig. 2: (a) EDS spectra of Sn-doped hematite thin films with various ALD cycle ratios and (b) EDS elemental maps of the film with an ALD cycle ratio 1:5. (c) EELS spectrum of the film with an ALD cycle ratio 1:20 after background subtraction and (d) the chemical shift of the Fe-L_3 edge between undoped hematite and Sn-doped hematite with an ALD cycle ratio 1:5.

position [28]. The fraction of Fe^{2+} ions was then obtained by linearly interpolating their peak chemical shift. As shown in Table 2, the Fe^{2+} concentration increases more moderately as the Sn concentration in hematite increases.

3.1.3 Theoretical understanding from DFT + *U* calculations

To gain insight into the effect of higher Sn concentrations on the properties of hematite we have performed density functional theory calculations with a Hubbard *U* parameter. Three different Sn concentrations were selected: 8.33, 16.67 and 33.33 mol%. Different distributions were studied in the 30-atom unit cell for 16.67 and 33.33 mol%. Their respective lowest energy configurations are displayed in Figure 3, with their corresponding electronic properties including oxidation states of iron and the evolution of lattice parameters with Sn-concentration. In our previous work [16], we have shown that doping with a single Sn^{4+} ion in the 30-atom α-Fe_2O_3 unit cell (8 mol% doping, which is close to the experimental value of 6 mol% in Table 2) turns Fe^{3+} in the neighbouring cation layer to Fe^{2+}. A similar effect was also previously observed for Ti-doped hematite [29]. The additional 3*d*-electron forms a localized band just below the Fermi-level (cf. density of states

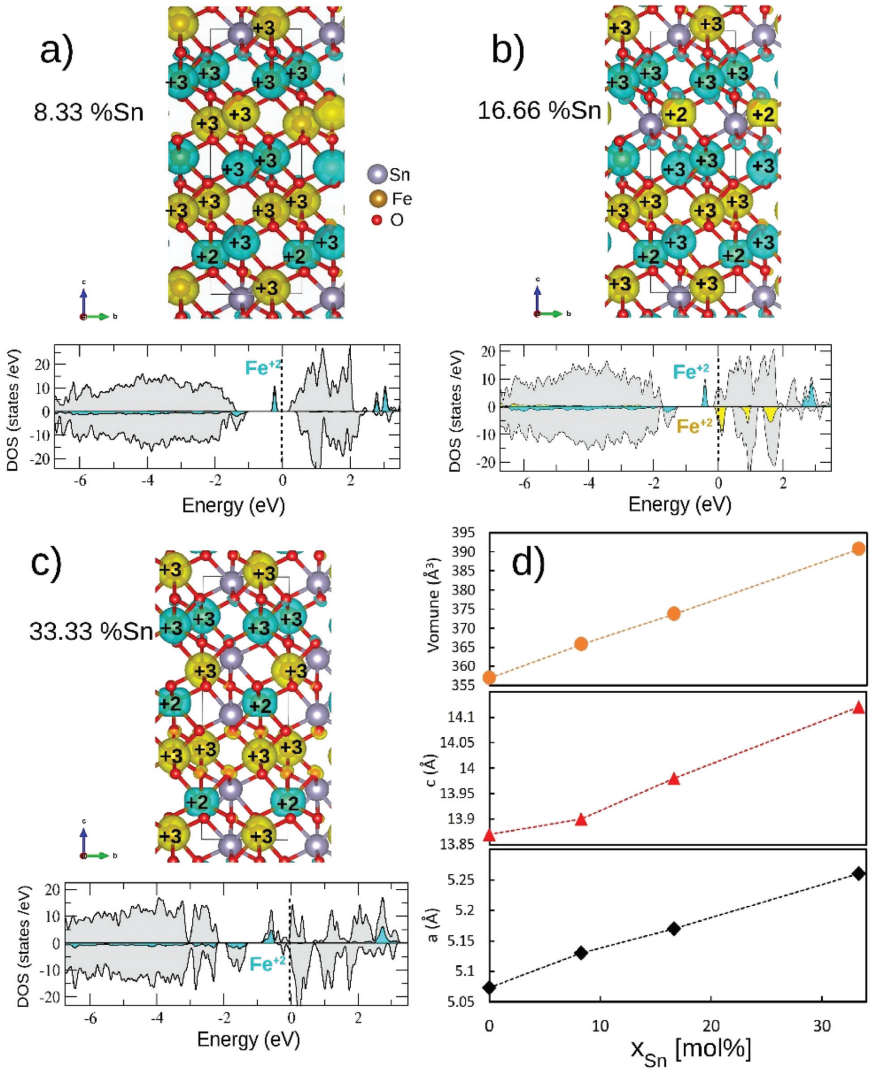

Fig. 3: Side view and spin density of Sn-doped hematite with Sn concentration of (a) 8.33, (b) 16.67, and (c) 33.33 mol%. Fe^{3+} (d^5) and Fe^{2+} (d^6) sites possess nearly spherical and flattened spin density, respectively. Fe, Sn, and O atoms are, respectively marked by orange, grey, and red spheres. Majority and minority spin density is marked in yellow and cyan, respectively. The corresponding density of states shows a reduction of the band gap due to localized states in the gap related to the sixth electron at Fe^{2+}. The partial density of states of Fe^{2+} is highlighted in yellow and cyan depending on the sign of the magnetic moment. (d) Volume and lattice parameters of hematite as a function of Sn concentration.

in Figure 3a). Analysis of oxidation states and electronic properties in Figure 3b–c shows that further increase of the Sn amount leads to a corresponding enhancement of the Fe^{2+} concentration (in line with the experimental measurement in Table 2) and reduction of the band gap. At 17 mol% Sn in Figure 3b, the localized band of one of the Fe^{2+} ions is close to the conduction band minimum. At 33 mol%, the Fermi level crosses the conduction band minimum and leads to *n*-type conductivity. The DFT+*U* calculations render a monotonic increase of the lattice parameters and the volume (cf. Figure 3d). Overall the DFT+*U* values are higher than in the experiments, likely due to the overestimation of lattice parameters typical for the GGA-PBE96 exchange correlation functional together with a Hubbard *U* correction. Moreover, while we have considered here substitutional doping of Sn, cation vacancies may also form to compensate the charge mismatch between Fe^{3+} and Sn^{4+} as an alternative to Fe^{3+} reduction.

3.2 Crystallinity of ALD Sn-doped hematite

In addition to phase determination, XRD was applied to study the crystallinity of the hematite thin films. The grazing incidence geometry for in-plane XRD makes it very sensitive to the surface alignment and its area, and hence not suitable to examine crystallinity. In our previous study [16], we have relied on the Bragg–Brentano geometry (θ-2θ scans) as well as out-of-plane pole figure measurements to evaluate the crystallinity. As shown in the (1,0,−1,4) pole figures (Figure 4), an apparent fiber texture is only observed in the hematite films without and with 6 mol% Sn (ALD cycle ratio 1:20). For the higher Sn concentrations, the pole figures become noisier, suggesting a decrease in the crystallinity.

In real space, the decrease in crystallinity is manifested by the decrease in grain sizes. As shown in the STEM micrograph (Figure 5a), the hematite thin films

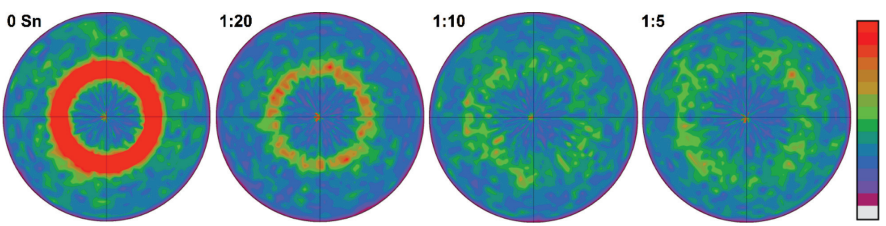

Fig. 4: XRD (1,0,−1,4) pole figures of Sn-doped hematite thin films with various ALD cycle ratios.

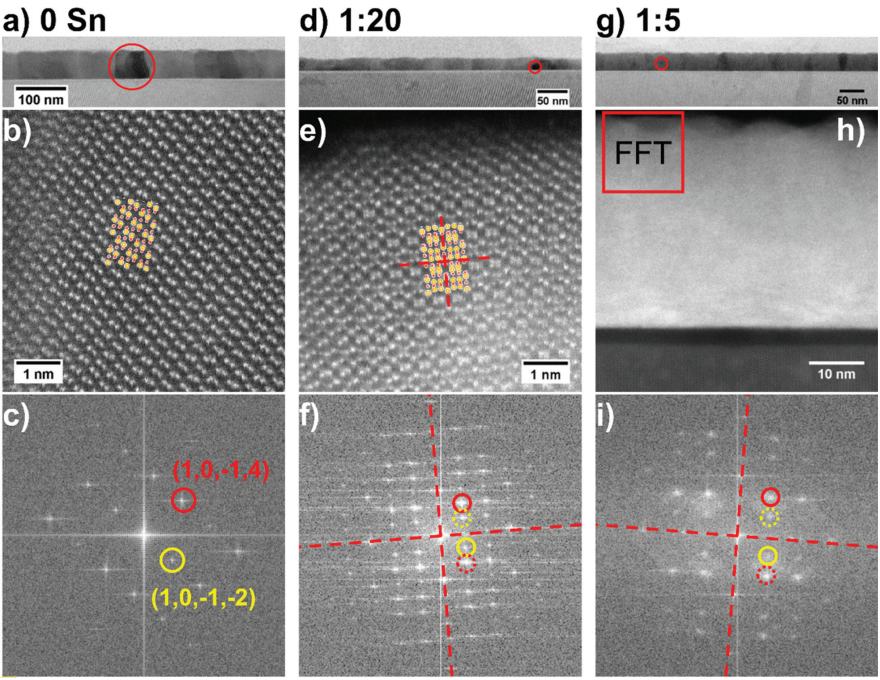

Fig. 5: STEM images of hematite films (a–c) without Sn doping, (d–f) with 6 mol% Sn (ALD cycle ratio 1:20), and (g–i) with 32 mol% Sn (ALD cycle ratio 1:5). The first row shows ABF-STEM images to identify some individual grains as highlighted by the red circles. The second row shows atomic resolution HAADF-STEM images along the (1,−2,1,0) zone axis of hematite grains and twin boundaries. The atomic structure of hematite (Fe atoms in orange, O in red) and an overlaid twin are superimposed. The third row shows the FFT of their corresponding HAADF-STEM images with (1,0,−1,4) and (1,0,−1, −2) reflections marked by circles in red and yellow, and their twin variants marked by broken circles in their respective colors. The broken lines in (e–i) highlight the mirror symmetry of the twin.

have columnar grains, and each grain has a vertical size equal to the film thickness. The surface termination is a (0,0,0,6) plane as evident in Figure 5b and c, which is in agreement with the XRD texture measurement. For the Sn-doped sample, however, many grains no longer span from the substrate to the surface, as shown by the highlighted grains in Figure 5d and g. Moreover, it is observed that many hematite grains have a twin relationship. As an example, Figure 5e shows the left and right grains in a twin relationship, whereas the middle part of the micrograph captures an overlapped area with both orientations. It is clear from the fast Fourier transform (FFT) pattern in Figure 5f that the twins have the mirror symmetry on the (0,0,0,6) as well as the (3,0,−3,0) planes. Finally, for the high Sn concentration at 32 mol%, even smaller hematite grains are observed.

As the grain size is much below the thickness of the specimen, it is difficult to observe these grains in atomic resolution. Nevertheless, twins are evidenced by the FFT pattern in Figure 5i. As a common defect in hematite, twins are formed by dehydration of α-FeOOH [30], having a coherent boundary and a common oxygen sublattice.

Despite their chemical homogeneity, it is clear that the grains are smaller in the hematite films with higher Sn concentrations. This may be understood by the ALD process where the hematite layer deposition is more frequently interrupted by the SnO_2 deposition to realize higher Sn concentration. Nevertheless, the observed grain size is much bigger than the thickness of hematite deposition between the SnO_2 deposition (<1 nm). The calcination procedure is a determining factor to the crystallinity. A mild calcination temperature of 600 °C for 30 min was chosen for this set of samples, which has been demonstrated to promote short-range ($\sim$1 nm) diffusion to homogenize the Sn doping as well as to inhibit longer range diffusion [16]. While suitable for designing localized Sn doping profiles, such calcination does not result in highly crystallized films at higher Sn concentrations. Hematite has a melting point of 1565 °C. The temperatures during the ALD and the calcination processes do not exceed a homologous temperature of 0.5, which kinetically hinders the phase separation of oversaturated Sn.

Higher calcination temperatures of up to 800 °C [13–15] have been reported to produce hematite thin film photoanodes on FTO substrates. Under these circumstances, however, Sn was found to diffuse into the hematite even from the FTO substrate [13, 15]. Long range diffusion may also cause unwanted Sn segregation as Sn has a low solubility in Fe_2O_3 [17]. In a recent study on hematite sintered at 1300 °C [31], Sn was demonstrated to segregate at the grain boundaries between the sintered particles. We have previously demonstrated that a pure hematite underlayer can promote the crystalline growth of Sn-doped hematite on top [16]. Overall, we have observed that the crystallinity of the hematite phase decreases as the Sn concentration increases. This compares well with the behaviour of ultrathin hematite films grown on FTO substrates [16].

3.3 Photoelectrochemical water splitting

Cyclovoltammetry (CV) measurements were carried out on hematite thin film electrodes with various Sn concentrations in the dark and under illumination (Figure 6a, see Section 2.4 for further information). The photocurrent density at 1.23 V vs. RHE, calculated as the difference between the current density under illumination and the corresponding dark current density, peaks at $\sim$0.4 mA cm^{-2} for the film with an ALD cycle ratio of 1:100 (Figure 6b). Films with low ALD cycle ratios (1:40, 1:80, 1:100, 1:120, 1:150) overperform undoped hematite, which can

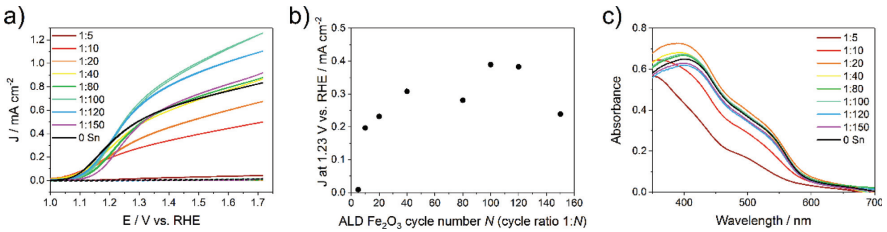

Fig. 6: (a) CV curves of Sn-doped hematite (colored) and undoped hematite (black) photoanodes measured under illumination (solid lines) and in the dark (respective dashed lines). (b) The calculated photocurrent density at 1.23 V vs. RHE. (c) Optical absorbance of hematite films on FTO with different Sn concentrations used in PEC experiments.

be attributed to improved electrical conductivity and charge separation properties [9, 12, 16]. On the other hand, films with higher Sn concentrations (ALD cycle ratios of 1:20, 1:10, 1:5) yield lower photocurrent density than undoped hematite.

As discussed in Section 3.2, the grain size of hematite decreases as the Sn concentration increases from 6 to 32 mol%. Crystallographic defects, including grain boundaries, are known to form trap states for charge carriers. Especially for hematite, a material known for slow hole transport, grain boundaries have been demonstrated to cause carrier recombination [6]. Additionally, films with high ALD cycle ratios of 1:10 and 1:5 show a significantly decreased optical absorbance in the visible range (Figure 6c). Therefore, we attribute the diminished PEC performance to both inferior crystallinity and a reduced absorbance with rising Sn concentration. As an outlook, it is also of interest to study the effect of dopants on the stability of hematite photoelectrodes by means of dissolution measurements [32, 33].

4 Conclusions

We present a study on the effect of Sn concentration on the microstructure and PEC water oxidation activity of hematite photoanodes. It is demonstrated that by ALD, up to 32 mol% Sn can be homogeneously incorporated into the hematite phase, which also leads to reduction of a fraction of Fe^{3+} to Fe^{2+}. The photocurrent peaks at an ALD cycle ratio of 1:100, whereas the photocurrent vanishes for a ratio of 1:5, which corresponds to 32 mol% Sn in hematite. The DFT+U results show that an increase of Sn content leads to an increase of Fe^{2+} concentration, which reduces the bandgap down to an n-type metallic state at 33 mol%. The theoretical results also confirm the increase of the lattice constants with Sn concentration found by in-plane XRD measurements. In addition, with the help of XRD

pole figures, we found that the crystallinity of the hematite thin film decreases with increasing Sn concentration, which is correlated to the observation of twin boundaries from STEM micrographs. The increase of grain boundary density and decrease in optical absorption may explain the reduction in PEC activity at Sn concentrations above 6 mol%. Nevertheless, these metastable films with high and homogeneous Sn incorporation may find applications making use of the lattice expansion and other solid solution effects. ALD is a promising way to synthesize similar oversaturated solid solution oxides, which can be explored as potential electrodes for photoelectrochemical water splitting.

Acknowledgment: We thank Dr Ramona Hoffmann and Dr Tristan Harzer for TEM sample preparation, and Merlin Junk for his contributions. We gratefully acknowledge the financial support by the Deutsche Forschungsgemeinschaft (DFG) within the Priority Program SPP 1613 (SolarH2) project and SFB/TRR247 (B4 and C4). AGH gratefully acknowledges funding by the Fonds der chemischen Industrie. We also acknowledge the grants for computational time at the Leibniz Rechenzentrum (grant pr87ro) and at magnitUDE of the Center of Computational Science and Simulation (DFG grant INST 20876/209-1 FUGG).

References

1. K. L. Hardee, A. J. Bard, J. Electrochem. Soc. **123** (1976) 1024.
2. K. Sivula, F. Le Formal, M. Gräztel, ChemSusChem **4** (2011) 432.
3. J. H. Kennedy, K. W. Frese Jr., J. Electrochem. Soc. **125** (1978) 709.
4. R. van de Krol, Y. Liang, J. Schoonman, J. Mater. Chem. **18** (2008) 2311.
5. A. Kay, I. Cesar, M. Grätzel, J. Am. Chem. Soc. **128** (2006) 15714.
6. U. Björksten, J. Moser, M. Grätzel, Chem. Mater. **6** (1994) 858.
7. L. Vayssieres, C. Sathe, S. M. Butorin, D. K. Shuh, J. Nordgren, J. Guo, Adv. Mater. **17** (2005) 2320.
8. R. Shinar, J. H. Kennedy, Solar Energy Mater. **6** (1982) 323.
9. A. Mettenbörger, Y. Gönüllü, T. Fischer, T. Heisig, A. Sasinska, C. Maccato, G. Carraro, C. Sada, D. Barreca, L. Mayrhofer, M. Moseler, A. Held, S. Mathur, Nano Energy **19** (2016) 415.
10. K. D. Malviya, H. Dotan, D. Shlenkevich, A. Tsyganok, H. Mor, A. Rothschild, J. Mater. Chem. A **4** (2016) 3091.
11. N. T. Hahn, C. B. Mullins, Chem. Mater. **22** (2010) 6474.
12. H. K. Dunn, J. M. Feckl, A. Müller, D. Fattakhova-Rohlfing, S. G. Morehead, J. Roos, L. M. Peter, C. Scheu, T. Bein, Phys. Chem. Chem. Phys. **16** (2014) 24610.
13. Y. Ling, G. Wang, D. A. Wheeler, J. Z. Zhang, Y. Li, Nano Lett. **11** (2011) 2119.
14. C. D. Bohn, A. K. Agrawal, E. C. Walter, M. D. Vaudin, A. A. Herzing, P. M. Haney, A. A. Talin, V. A. Szalai, J. Phys. Chem. C **116** (2012) 15290.

15. B. Wickman, A. Bastos Fanta, A. Burrows, A. Hellman, J. B. Wagner, B. Iandolo, Sci. Rep. **7** (2017) 40500.
16. A. G. Hufnagel, H. Hajiyani, S. Zhang, T. Li, O. Kasian, B. Gault, B. Breitbach, T. Bein, D. Fattakhova-Rohlfing, C. Scheu, R. Pentcheva, Adv. Funct. Mater. **28** (2018) 1804472.
17. M. Takano, Y. Bando, N. Nakanishi, M. Sakai, H. Okinaka, J. Solid State Chem. **68** (1987) 153.
18. J. Z. Jiang, R. Lin, S. Morup, K. Nielsen, F. W. Poulsen, F. J. Berry, R. Clasen, Phys. Rev. B **55** (1997) 11.
19. B. M. Klahr, A. B. Martinson, T. W. Hamann, Langmuir, **27** (2011) 461.
20. G. Kresse, J. Hafner, Phys. Rev. B **49** (1994) 14251.
21. G. Kresse, J. Furthmüller, Comput. Mater. Sci. **6** (1996) 15.
22. G. Kresse, J. Furthmüller, Phys. Rev. B **54** (1996) 11169.
23. P. Blöchl, Phys. Rev. B **50** (1994) 17953.
24. J. P. Perdew, K. Burke, M. Ernzerhof, Phys. Rev. Lett. **77** (1996) 3865.
25. S. L. Dudarev, G. A. Botton, S. Y. Savrasov, C. J. Humphreys, A. P. Sutton, Phys. Rev. B **57** (1998) 1505.
26. H. J. Monkhorst, J. D. Pack, Phys. Rev. B **13** (1976) 5188.
27. S. Zhang, C. Scheu, Microscopy, **67** (2018) i133.
28. P. A. van Aken, B. Liebscher, Phys. Chem. Miner. **29** (2002) 188.
29. R. Pentcheva, H. Sadat Nabi, Phys. Rev. B **77** (2008) 172405.
30. F. Watari, J. van Landuyt, P. Delavignette, S. Amelinckx, N. Igata, Phys. Stat. Sol. A **73** (1982) 215.
31. M. R. S. Soares, C. A. R. Costa, E. M. Lanzoni, J. Bettini, C. A. O. Ramirez, F. L. Souza, E. Longo, E. R. Leite, Adv. Electr. Mater. **5** (2019) 1900065.
32. J. Knöppel, S. Zhang, F. D. Speck, K. J. J. Mayrhofer, C. Scheu, S. Cherevko, Electrochem. Commun. **96** (2018) 53.
33. S. Zhang, M. Rohloff, O. Kasian, A. M. Mingers, K. J. J. Mayrhofer, A. Fischer, C. Scheu, S. Cherevko, J. Phys. Chem. C **123** (2019) 23410.